nature materials

ARTICLES

PUBLISHED ONLINE: 13 NOVEMBER 2017 | DOI: 10.1038/NMAT5024

Mechanotransduction-modulated fibrotic microniches reveal the contribution of angiogenesis in liver fibrosis

Longwei Liu[1,2†], Zhifeng You[1†], Hongsheng Yu[1], Lyu Zhou[1,2], Hui Zhao[1,2], Xiaojun Yan[1], Dulei Li[3], Bingjie Wang[1,2], Lu Zhu[1], Yuzhou Xu[4], Tie Xia[3], Yan Shi[3], Chenyu Huang[5], Wei Hou[6] and Yanan Du[1*]

The role of pathological angiogenesis on liver fibrogenesis is still unknown. Here, we developed fibrotic microniches (FμNs) that recapitulate the interaction of liver sinusoid endothelial cells (LSECs) and hepatic stellate cells (HSCs). We investigated how the mechanical properties of their substrates affect the formation of capillary-like structures and how they relate to the progression of angiogenesis during liver fibrosis. Differences in cell response in the FμNs were synonymous of the early and late stages of liver fibrosis. The stiffness of the early-stage FμNs was significantly elevated due to condensation of collagen fibrils induced by angiogenesis, and led to activation of HSCs by LSECs. We utilized these FμNs to understand the response to anti-angiogenic drugs, and it was evident that these drugs were effective only for early-stage liver fibrosis *in vitro* and in an *in vivo* mouse model of liver fibrosis. Late-stage liver fibrosis was not reversed following treatment with anti-angiogenic drugs but rather with inhibitors of collagen condensation. Our work reveals stage-specific angiogenesis-induced liver fibrogenesis via a previously unrevealed mechanotransduction mechanism which may offer precise intervention strategies targeting stage-specific disease progression.

Fibrotic diseases account for ∼45% of deaths in industrialized countries[1], which are accompanied with pathological angiogenesis in multiple organs[2,3]. In liver, sinusoid angiogenesis with an abnormal angioarchitecture is a hallmark related to liver fibrogenesis, which implicates a potential target for therapeutic interventions[4,5]. However, the efficacy of anti-angiogenesis therapy on liver fibrosis has been controversial so far. For example, tyrosine-kinase inhibitors such as Sorafenib have been proved to block sinusoid remodelling and facilitate liver fibrosis resolution[6–8], while other anti-angiogenic interventions such as Cilengitide had detrimental effects[5,9]. Moreover, sinusoid angiogenesis promoted by myeloid cell-derived vascular endothelial growth factor (VEGF) was even shown to promote liver fibrosis resolution[10,11]. Collectively, these contradictory reports imply the unclarified impacts and mechanisms of pathological sinusoid angiogenesis in the context of liver fibrogenesis and relevant therapeutic interventions.

Clinically, liver fibrosis could be divided into multiple stages, such as F0–F4 in the METAVIR system[12]. In the early stage, fenestrated liver sinusoid endothelial cells (LSECs) undergo defenestration and form basement membrane[13]. Meanwhile, their inhibitory effects on HSC activation in physiological conditions[14] are hampered[13,15], leading to HSC activation, extracellular matrix (ECM, mainly collagen I) synthesis, remodelling, and subsequent tissue stiffening. In the late stage, myofibroblast-mediated tissue remodelling persists and sinusoid rarefication is prominent, which is mainly comprised of acellular scars[11,12]. Based on the stage-dependent status of angiogenesis, we hypothesize that the influences of angiogenesis on HSC activation and liver fibrogenesis vary at different fibrotic stages, which may be the cause of controversy over therapeutic interventions.

Previously reported *in vitro* fibrosis models were usually based on LSECs and HSCs co-culture lacking physiological interactions, mainly focused on the biochemical contribution of paracrine vascular factors, such as endothelin and nitrogen oxide, on HSC activation and ECM remodelling during fibrosis progression[16]. Recently, advances in the emerging field of mechanobiology have revealed that ECM-mediated mechanotransduction could modulate inflammation and fibrosis[17]. Mechanical strain generated during ECM remodelling has been shown to direct angiogenesis[18]. Meanwhile, ECM provides a binding scaffold for endothelial cell anchorage and migration during angiogenesis, and the cell–ECM interaction generates mechanical strain[19–21]. However, to the best of our knowledge, no study has been conducted on how mechanical tension generated during angiogenesis influences the progression of liver fibrosis. In this work, *in vitro* three-dimensional-biomimic FμNs containing either human or primary mouse LSECs and HSCs were applied along with an *in vivo* anterior chamber model to convincingly reveal a previously unreported scheme for angiogenesis-induced HSC activation from a mechanobiological perspective and in a stage-dependent manner.

Sinusoid angiogenesis at different stages of liver fibrosis

To characterize the pathological sinusoid angiogenesis at different stages of liver fibrosis, human liver samples with varying severity

[1]Department of Biomedical Engineering, School of Medicine, Collaborative Innovation Center for Diagnosis and Treatment of Infectious Diseases, Tsinghua University, Beijing 100084, China. [2]School of Life Sciences, Tsinghua University, Beijing 100084, China. [3]Institute for Immunology, School of Medicine, Tsinghua University, Beijing 100084, China. [4]Sequencing core facility, Tsinghua University, Beijing 100084, China. [5]Department of Dermatology, Beijing Tsinghua Changgung Hospital, Tsinghua University, Beijing 102218, China. [6]Tianjin Second People's Hospital and Tianjin Institute of Hepatology, Tianjin 300192, China. †These authors contributed equally to this work. *e-mail: duyanan@tsinghua.edu.cn

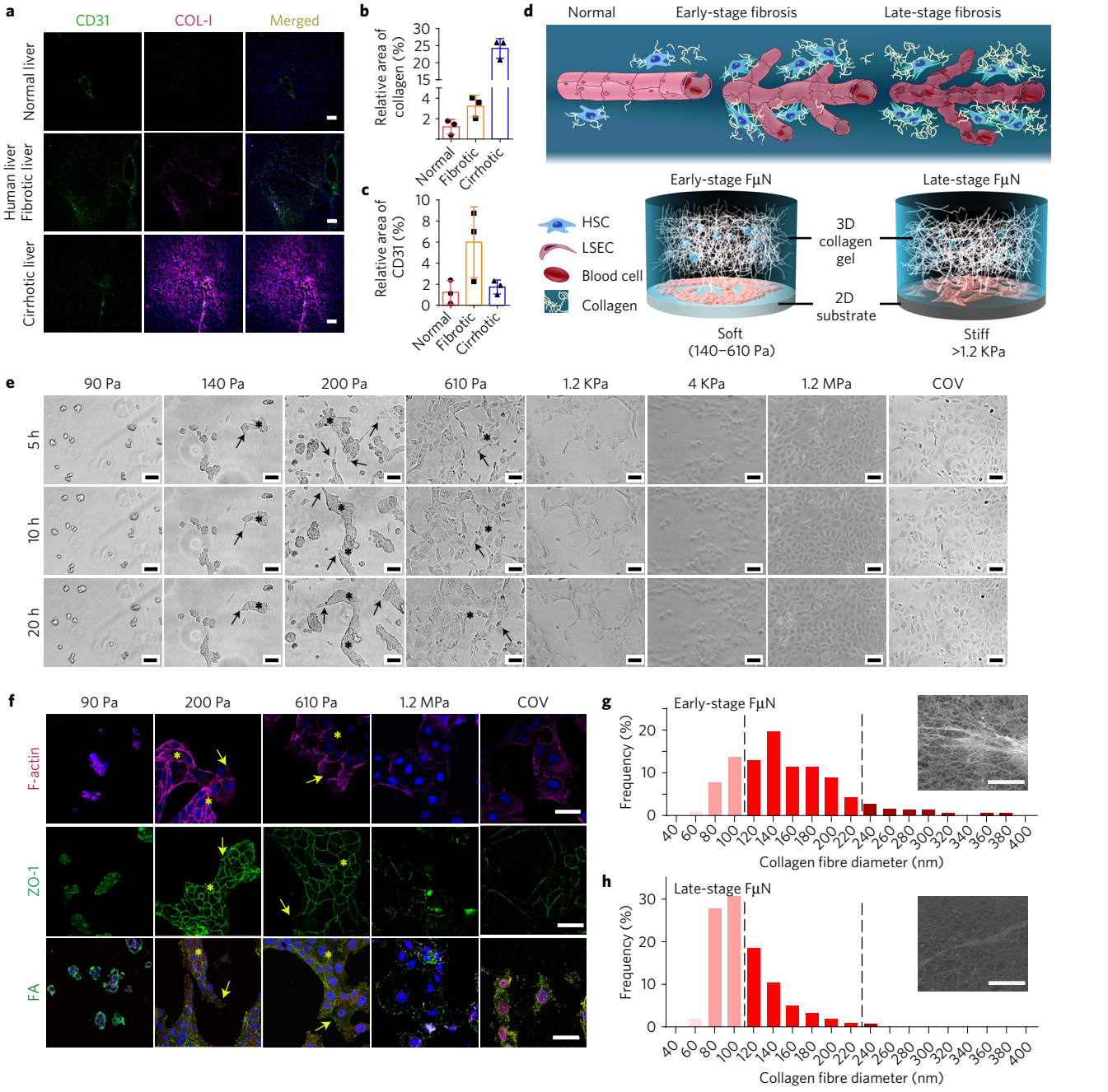

Figure 1 | Establishment of the mechanotransduction-modulated fibrotic microniches (FμNs). a–c, Representative images and quantification of co-immunofluorescent staining of CD31 (green) and collagen I (magenta) in human liver specimens at different stages of liver fibrosis, indicating the changes of sinusoid angiogenesis during fibrosis progression ($n = 3$ in **b**,**c**). Blue, nuclear. Scale bar, 100 μm. **d**, Schematic drawing to illustrate the conceptual design of the biomimetic FμNs to recapitulate the spatial organization and dynamic interactions of LSECs and HSCs in hepatic sinusoids, as well as ECM remodelling during hepatic fibrosis progression. **e**, Time-lapse images of human LSECs on substrates with different stiffness. Asterisks for stalk cells, arrows for tip cells. Scale bar, 100 μm. **f**, Representative immunofluorescent images of cytoskeleton (F-actin), focal adhesion (FA) complex (paxillin and vinculin) and cell-junction protein (ZO-1). Blue, nuclear. Asterisks for stalk cells, arrows for tip cells. Scale bar, 100 μm. **g**,**h**, Quantification of collagen fibre diameters and distribution frequency in early-stage (**g**) and late-stage (**h**) FμNs (300 collagen fibres were analysed). Scale bar, 10 μm. Data are expressed as mean ± s.d.

of fibrosis were harvested and analysed (Supplementary Fig. 1a). Increased accumulation of collagen fibres was associated with the exacerbation of liver fibrosis (Fig. 1a,b). Meanwhile, a sharp increase in sinusoid angiogenesis during early-stage fibrosis was observed, which gradually diminished along with the formation of insoluble scars in late-stage fibrotic livers (Fig. 1a,c). Similar results were observed in carbon tetrachloride (CCL_4)-induced liver fibrosis mouse models (Supplementary Fig. 1b–d). These data showed that sinusoid angiogenesis status underwent dynamic changes at different stages of liver fibrosis.

Mechanotransduction-modulated FμNs *in vitro*

To find out how sinusoid angiogenesis influences the progression of liver fibrosis at different stages, a series of FμNs were established to recapitulate the spatial organization and dynamic interactions of LSECs and HSCs in hepatic sinusoids, as well as ECM remodelling

during fibrosis progression (Fig. 1d). FμNs were constituted of LSECs cultured on underlying two-dimensional (2D) substrates with tailored stiffness (Fig. 1e, Supplementary Fig. 2a,b and Supplementary Discussion), and overlaid three-dimensional (3D) collagen (Type I) hydrogel embedded with HSCs. Only when LSECs were cultured on polyethylene glycol (PEG) hydrogel substrates with stiffness in the range 140–610 Pa could they migrate collectively to form capillary-like structures, as typically seen in sinusoid angiogenesis during early-stage liver fibrosis (Fig. 1e, Supplementary Fig. 4a and Supplementary Movies 2 and 4). The best capillarization was realized on a substrate of 200 Pa, which is regarded as the optimal stiffness. These migratory LSECs exhibited super-cellular organization with tip cell migration followed by the stalk cells, leading to the formation of basement membrane (Supplementary Fig. 3a). Actin stress fibres in the tip cells and cortical actin rim in the stalk cells could be visualized along with focal adhesion expressed mainly around lamellipodia, which may generate directional forces to drive the collective migration of LSECs[22] (Fig. 1f). In contrast, LSECs cultured on harder substrates with stiffness >1.2 kPa, as represented by coverslip (COV), showed random migration (Fig. 1e and Supplementary Movie 3) with stress actin fibre and sparsely distributed focal adhesion complexes (Fig. 1f). These LSECs recapitulated traits of hardened and leaky sinusoids in late-stage fibrotic or cirrhotic livers[23,24], as represented by enlarged nuclear distances (Supplementary Fig. 3b) as well as the loss of endothelial adherent junction protein ZO-1 (Fig. 1f)[25]. For simplification, we denoted FμNs established on 200 Pa hydrogel substrate as 'early-stage FμNs' and those established on COV as 'late-stage FμNs'. In addition, collective migration of LSECs on 200 Pa substrates was not disturbed by 3D collagen gel overlay during early-stage FμNs construction (Supplementary Movie 5), which induced stronger collagen remodelling than the LSECs in late-stage FμNs (Fig. 1g,h).

Gene differential analysis of LSECs *in vitro* and *in vivo*

To investigate whether the *in vitro* mechanobiologically modulated LSECs could reflect the pathological progression of LSECs during liver fibrosis, primary mouse LSECs from healthy liver (N) and fibrotic liver exposed to CCL_4 induction for 3 weeks (3W, early-stage) and 10 weeks (10W, late-stage) were isolated and characterized by RNA-Seq (Fig. 2a). Differentially expressed genes (DEGs) analysis revealed drastic changes of LESCs during *in vitro* culture (N versus 200 Pa versus COV) and during fibrosis progression *in vivo* (N versus 3W versus 10W) (Fig. 2b and Supplementary Fig. 5a,b). To check the similarity of LSECs *in vitro* and *in vivo*, genes significantly changed in both early- and late-stage LSECs were matched, which would also facilitate identification of important pathways and related genes that mediated LSECs phenotypic changes at different fibrotic stages. 64.2% and 68.7% significantly upregulated genes in early-stage and late-stage LSECs *in vivo* were also upregulated *in vitro*, respectively. Meanwhile, 74.4% and 88.5% significantly downregulated genes in early-stage and late-stage LSECs *in vivo* were also downregulated *in vitro*, respectively (Fig. 2c).

In particular, we compared gene expression of angiogenesis-related signalling pathways such as ECM–receptor interactions and focal adhesion signalling[26] and fibrosis-related signalling pathways such as chemokine signalling[27] and cytokine–cytokine receptor interaction[28], which showed high similarity between different *in vitro* and *in vivo* counterparts (Fig. 2d,e and Supplementary Fig. 6a–d). Collectively, mechanobiologically modulated LSECs in FμNs could largely recapitulate the featured genetic changes of LSECs during fibrosis progression *in vivo*.

HSC activation and ECM modelling in FμNs

To investigate how LSECs in different FμNs influence fibrosis progression, activation of HSCs was characterized in terms of contractility, fibrogenesis, proliferation and FμN stiffening (Fig. 2f). Collagen contraction assay revealed an elevated cell-generated contractile force in early-stage FμNs compared to that in late-stage FμNs for both human and primary mouse LSECs and HSCs (Fig. 2g and Supplementary Fig. 4b,c). Furthermore, elevated expression of αSMA (marked by αSMA-GFP reporter) was observed in early-stage FμNs, indicating HSC activation (Fig. 2h,i). Similar results were seen at both gene and protein levels (Fig. 2j,k). Meanwhile, stiffness of early-stage FμNs was significantly increased compared to late-stage FμNs due to condensation of the remodelled collagen (Fig. 2l). Rapid proliferation of HSCs was demonstrated by elevated expression of Ki-67 in early-stage rather than in late-stage FμNs (Fig. 2m). These results implied that HSCs could be activated by LSECs in early-stage liver fibrosis but were less responsive in the later stage.

Remodelled collagen fibre-mediated HSC activation

To investigate whether paracrine factors alone could contribute to HSC activation, live LSECs were replaced with PFA-fixed LSECs in early-stage FμNs and supplemented with conditional medium (CM) from LSECs (separately cultured on 200 Pa hydrogel substrate for 1 day) as paracrine factors, which did not result in significant contraction (Fig. 3a,b,f). Furthermore, a Transwell set-up (Fig. 3c) was established, enabling dynamic paracrine exchange between HSCs and LSECs (in adjacent wells) while excluding physical contraction of LSECs (using PFA-fixed LSECs) in the FμNs. The paracrine factors dynamically secreted from physically separated LSECs could not induce significant collagen remodelling and activation of HSCs (Fig. 3c,f). We then embedded both HSCs and PFA-fixed LSECs in collagen gel to enable physical cell–cell contact in the presence of CM, which did not lead to contraction either (Fig. 3d,f). Furthermore, these two types of cells showed rare direct cell–cell contact in early-stage FμNs (Supplementary Movie 6), suggesting that physical contact plus paracrine factors were insufficient for HSC activation.

Interestingly, 3D collagen gel could be contracted by the underlying LSECs alone (Supplementary Fig. 7a), implying that the collectively migratory LSECs might contribute to collagen contraction in early-stage FμNs. Blebbistatin (Bleb), a myosin II inhibitor, was applied to pre-treat LSECs on 200 Pa substrate for inhibition of their contractility and migration, which could significantly impede collagen contraction (Fig. 3e,f). All these factors implied that the mechanical force exerted by LSECs was indispensable for HSC activation and tissue remodelling. Besides, fixed collagen gel with restricted remodelling would hinder the activation of HSCs (Supplementary Fig. 7c). The activated HSCs (αSMA^+) were co-localized with condensed collagen fibres and collectively migratory LSECs in early-stage FμNs (Fig. 3g,h). Meanwhile, fewer collagen fibrils were remodelled in late-stage FμNs. Activated HSCs (αSMA^+) were present adjacent to the condensed collagen fibres and vasculature ($CD31^+$) in CCL_4-induced fibrotic mouse livers and in human fibrotic liver specimens (Fig. 3i and Supplementary Fig. 7d,e). The above data suggested that LSECs and collagen fibres were involved in HSC activation both *in vitro* and *in vivo*. In addition, integrin β1 knockdown in LESCs could reduce collagen remodelling, implying that LSECs could modulate collagen fibrils via integrin receptors (Supplementary Fig. 7f).

Next, the anterior chamber angiogenesis model was adopted as a simplified *in vivo* model to further validate our hypothesis on angiogenesis-mediated activation of HSCs. Angiogenesis inductive material (AIM) was fabricated based on a PEG microscaffold loaded with bFGF-encapsulated alginate hydrogel (Fig. 3j and Supplementary Fig. 8a). The control-released bFGF could induce angiogenesis without fibroblast activation[29] (Supplementary Fig. 8b,c). Upon implantation into the mouse eye, AIM could induce extensive angiogenesis in the anterior chamber within five days (Fig. 3k).

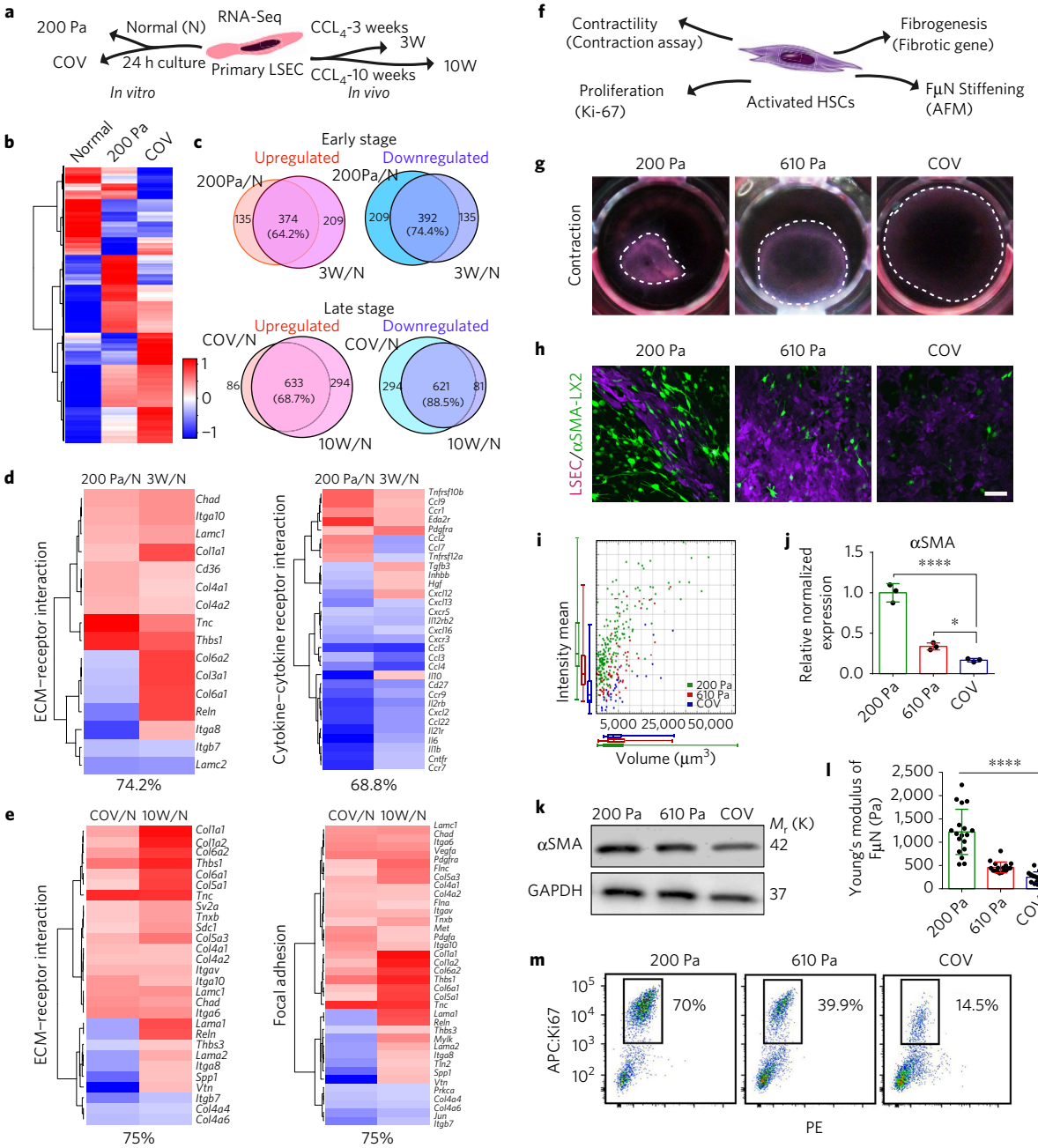

Figure 2 | Characterization of the biomimetic FμNs. a, Illustration of *in vitro* and *in vivo* sample preparation for RNA-seq. **b**, Heat map of DEGs *in vitro* (DEGs, q-value < 0.01, $\log_2$ FC > 1 or < −1; value bar indicates the TPM (Z-score) for each gene). **c**, Venn diagrams of DEGs *in vitro* (200 Pa and COV compared to normal LSECs (N), respectively) and *in vivo* (3W and 10W compared to N, respectively) from early- and late-stage LSECs (DEGs, q-value < 0.01, $\log_2$ FC > 1 or < −1). (Similarity between each two conditions is shown as a percentage.) **d**,**e**, Heat map of DEGs in different signalling pathways between *in vitro* and *in vivo*. (Bottom percentage indicates the similarity between *in vitro* and *in vivo*. DEGs, q-value < 0.01, $\log_2$ FC > 1 or < −1. Value bar indicates the $\log_2$FC for each gene.) **f**, Characterization of activated HSCs in terms of tissue contraction, fibrogenesis and proliferation, and FμN stiffening. **g**, Remodelling of FμNs mimicking different stages of liver fibrosis. **h**, Maximum intensity projection of a 3D confocal image of FμNs. (Z = 200 μm. Magenta represents the human LSECs carrying a CMV-mCherry reporter and green represents LX-2 carrying αSMA-GFP reporter. Scale bar, 100 μm.) **i**, Quantification of αSMA-GFP fluorescence and cell volume in **h**. **j**,**k**, αSMA expression in different FμNs at gene (**j**) and protein (**k**) level (n = 3, one-way analysis of variance (ANOVA), *P = 0.0265, ****P < 0.0001 in **j**). **l**, Young's modulus of FμNs established with different substrates (n = 12, one-way ANOVA, ****P < 0.0001). **m**, Analysis of proliferating LX2 cells in FμNs by Ki-67 staining. Data are expressed as mean ± s.d.

After angiogenic induction, FITC-conjugated collagen encapsulated with αSMA-mCherry reporter-labelled HSCs was injected into the vascularized anterior chamber. Condensation of collagen fibrils and intensified activation of HSCs were observed three days after implantation (Fig. 3l,m), indicating that angiogenesis could activate HSCs through condensation of collagen fibrils.

HSC activation via collagen-mediated mechanotransduction

Since the contraction force induced by a single cell was estimated to be ∼10 nN (ref. 30), a mechanical strain of ∼200 nN, applied by atomic force microscopy (AFM), representing multiple-cell collective stretching during angiogenesis was used as substitute for LSECs-exerted stretching of collagen fibrils to investigate

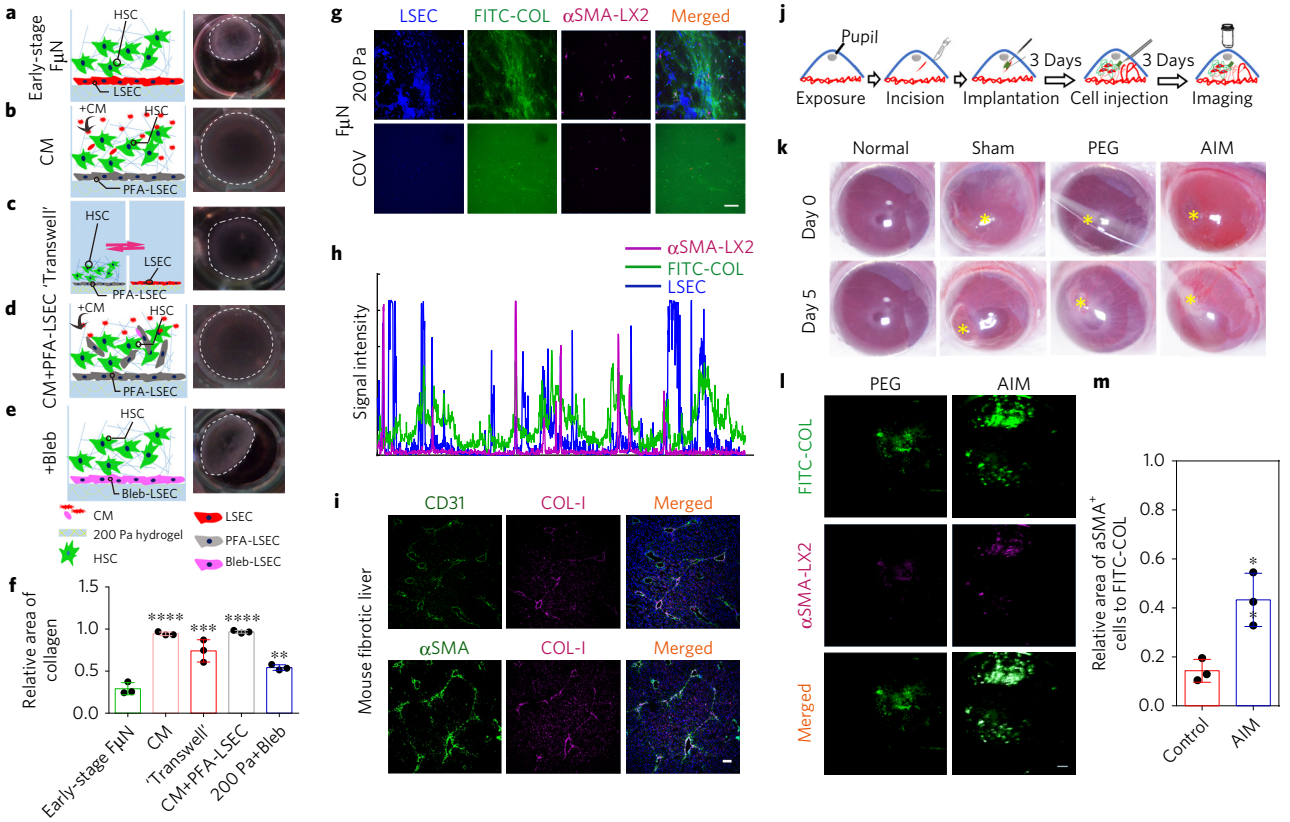

Figure 3 | Condensed collagen fibres as mechanical transducer to activate HSCs both *in vitro* and *in vivo*. **a**, Early-stage FμNs as the positive control. **b**, FμNs established using PFA-fixed LSECs and supplemented with CM collected from 200 Pa cultured LSECs. **c**, 'Transwell' to maintain paracrine exchange without direct cell–cell contacts. **d**, PFA-fixed cells directly embedded in hydrogel and supplemented with CM to recreate physical cell–cell contacts. **e**, FμNs established using blebbistatin pre-treated LSECs to inhibit migration. **f**, Quantification of collagen area after remodelling ($n=3$ in each group, one-way ANOVA, $^{****}P<0.0001$, $^{***}P=0.0001$, $^{****}P<0.0001$ and $^{**}P=0.0092$, respectively). **g**, Co-localization of migratory LSECs with condensed collagen fibres and activated HSCs in early-stage FμNs. Scale bar, 200 μm. **h**, Plot profile analysis of early-stage FμNs showed the co-localization of collectively migratory LSECs, condensed collagen fibres and activated HSCs. **i**, Representative immunofluorescent images of CD31, αSMA and collagen I in mouse fibrotic liver. Blue, nuclear. Scale bar, 100 μm. **j**, Schematic of anterior chamber angiogenesis model. **k**, Bright-field images of mouse eye at day 0 and day 5. Asterisk indicates the operation and implantation site. **l**, Representative *Z*-stacked confocal images of eyes implanted with control material or AIM ($Z=1{,}270$ μm). Scale bar, 100 μm. **m**, Quantification of αSMA-mCherry signal in the control and AIM groups, normalized to collagen fluorescence areas ($n=3$, two-tailed *t*-test, $^{*}P=0.0132$). Data are expressed as mean ± s.d.

mechano-transduced HSC activation (Fig. 4a and Supplementary Fig. 9a). To enable instantaneous monitoring of HSC activation, SRC biosensor was transfected to HSCs[31,32], whose phosphorylation as represented by ECFP signal could be correlated with HSC activation[33] (Supplementary Fig. 9b,c). Mechanical stretching applied by the AFM tip via collagen fibrils for 5 min alone could be sufficient to activate SRC phosphorylation in a single HSC (Fig. 4b,c), which was comparable to PDGF induction, a widely used mitogen for HSC activation[34] (Fig. 4d).

Mediators of collagen-mediated mechanotransduction

We then investigated downstream mediators of collagen-mediated mechanotransduction for HSC activation. As reported, membrane receptor DDR2 in HSCs is activated by interaction with collagen fibres which could enhance proliferation and migration of HSCs[35,36]. Elevated DDR2 expression was observed in αSMA^{+} HSCs in early-stage FμNs (Fig. 4e) as well as in early-stage fibrosis in mice (Supplementary Fig. 9g,h). To further confirm the DDR2-mediated HSC activation, we knocked down (KD) *DDR2* in HSCs (Supplementary Fig. 9i) by shRNA and applied bi-directional stretching to substitute the mechanical force exerted by LSECs (Fig. 4f). Activation of HSCs under stretching (Fig. 4g,h) or in early-stage FμNs (Supplementary Fig. 9j) were both impeded by DDR2-KD, suggesting that DDR2 was a downstream mediator of collagen-mediated mechanotransduction for HSC activation. JAK2/PI3K/AKT signalling has been previously reported in the downstream of DDR2 (ref. 37) and correlates with the transcription factor of αSMA, myocardin[38], which was hypothesized to be involved in DDR2-mediated mechanotransduction signalling. As expected, phosphorylation of JAK2, PI3K, AKT were all reduced after DDR2-KD (Fig. 4i). As a consequence, expression of myocardin and αSMA were downregulated (Fig. 4i). Furthermore, inhibitors to DDR2 (DDR1-IN-1), JAK2 (Runxolitinib), PI3K (ZSTK474) or AKT (MK-2206) could all reduce the expression of myocardin and αSMA in HSCs under stretching (Fig. 4j,k). Expression of αSMA could be also reduced after treatment with related inhibitors in early-stage FμNs (Fig. 4l,m).

All these data support a previously unreported mechanobiological mechanism governing collagen fibre-mediated HSC activation through the DDR2-JAK2/PI3K/AKT-myocardin signalling pathway, which ultimately promotes tissue remodelling and progression of liver fibrosis (Fig. 4n and Supplementary Movie 1).

Anti-angiogenesis therapy to early-stage liver fibrosis

With insights into the contribution of pathological sinusoid angiogenesis at different stages of liver fibrosis, we speculated that the success of anti-angiogenesis therapy would depend on the pathological status, which would be effective only in early-stage but

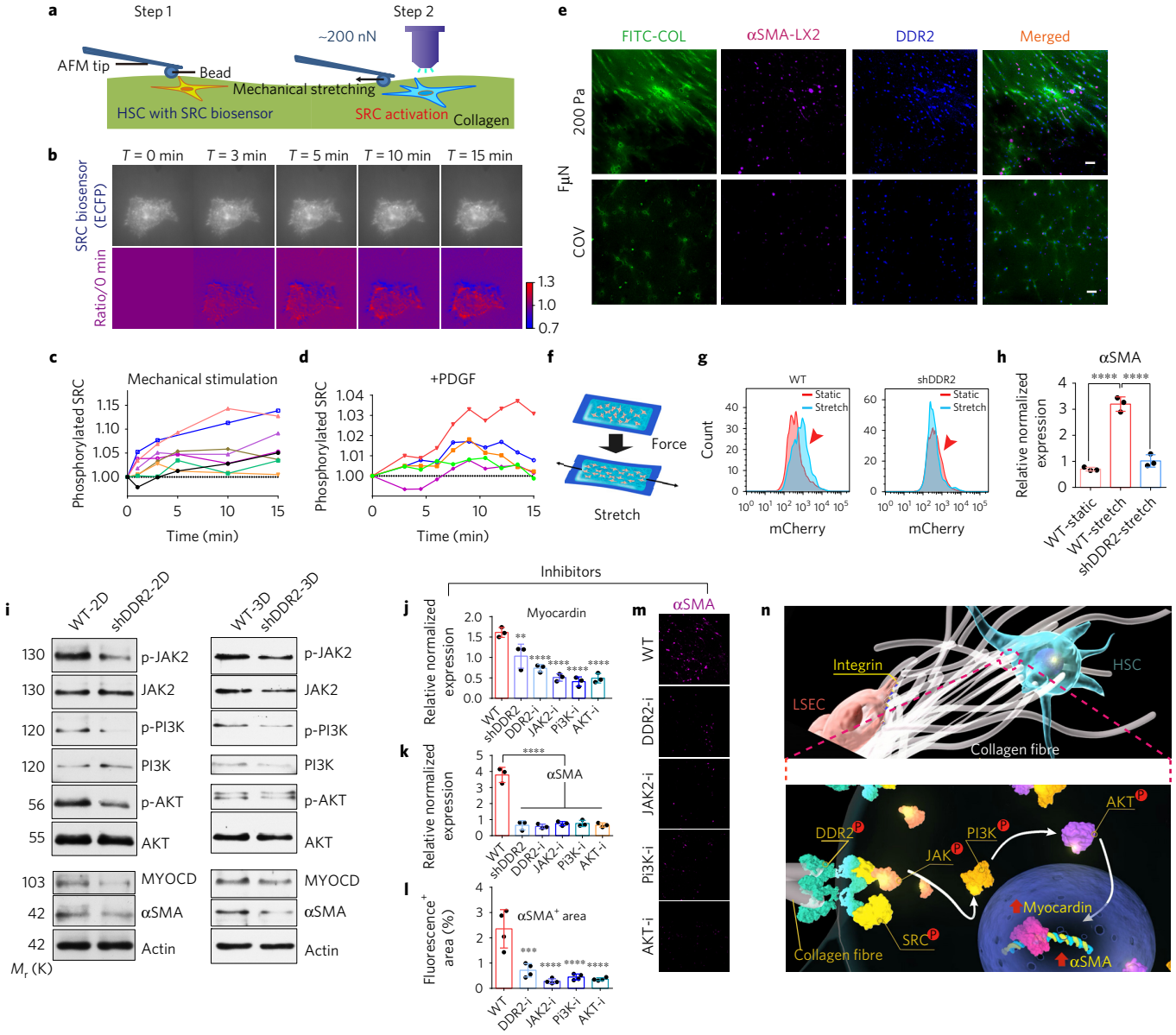

Figure 4 | Collagen fibres function as mechanical transducer to activate HSCs through the DDR2-JAK2/PI3K/AKT-MYOCD pathway. a, Schematic illustration of experimental design to monitor SRC activation via AFM-applied stretching at the single-cell level. Step 1, Anchoring an AFM bead to collagen fibrils adjacent to HSCs. Step 2, A mechanical strain of 200 nN was applied by AFM tip to the HSC through stretching collagen fibrils; meanwhile, change of SRC biosensor was monitored. **b**, Representative images and corresponding ratio changes (compared to 0 min) of phosphorylated SRC (ECFP) during 15 min stretching. **c**,**d**, Time-lapse expression of the phosphorylated SRC in HSCs in response to mechanical stimulation through collagen fibrils (**c**) and biochemical induction by PDGF (**d**). Each line represents one single cell. **e**, Representative immunofluorescent images of DDR2 in FμNs. Scale bar, 100 μm. **f**, Schematic of bi-directional stretching. **g**, Flow cytometry analysis of αSMA expression of WT and shDDR2 HSCs upon exposure to stretching (ST). **h**, αSMA gene expression of WT or shDDR2 LX2 upon stretching (ST) ($n = 3$, one-way ANOVA, $^{****}P < 0.0001$). **i**, Western blot analysis of key components in the DDR2 downstream signalling pathway, myocardin (MYOCD) and αSMA in WT HSCs and shDDR2 HSCs cultured on 2D substrate and within 3D collagen matrix subjected to stretching (ST). **j**,**k**, Gene expression of MYOCD (**j**) and ACTA2 (αSMA, **k**) after applying inhibitors of key components involved in the DDR2 downstream signalling pathway to HSCs cultured within 3D collagen matrix subjected to stretching (ST) ($n = 3$, one-way ANOVA, $^{**}P = 0.0036$, $^{****}P < 0.0001$). **l**,**m**, Expression of αSMA was significantly reduced after treatment with related inhibitors in early-stage FμNs. ($n = 4$, one-way ANOVA, $^{***}P = 0.001$, $^{****}P < 0.0001$). **n**, Schematic of collagen fibre-mediated HSC activation (MYOCD and SMA upregulation) via the DDR2-JAK2/PI3K/AKT pathway. Data are expressed as mean ± s.d.

not in late-stage liver fibrosis. We therefore tested the efficacy of two clinically administered drugs, Sorafenib (SORA) and Captopril (CAP), which have been both reported to have an anti-angiogenesis effect. Both drugs could significantly reduce early-stage FμNs remodelling *in vitro* (Fig. 5a). Furthermore, FμNs could be miniaturized to the 384 format for high-throughput *in vitro* drug testing (Fig. 5b–d and Supplementary Figs 10a–c and 11c,d). SORA and CAP showed effective inhibition of collagen contraction with varying half maximal inhibitory concentration of viability (ICV50) and half maximal inhibitory concentration of contraction (ICC50) (Fig. 5e). Meanwhile, when administered to mouse models with early-stage liver fibrosis, SORA, CAP as well as VEGFR2 neutralizing antibody for specific LSECs targeting could all significantly reverse early-stage fibrosis *in vivo* (Fig. 5f–h).

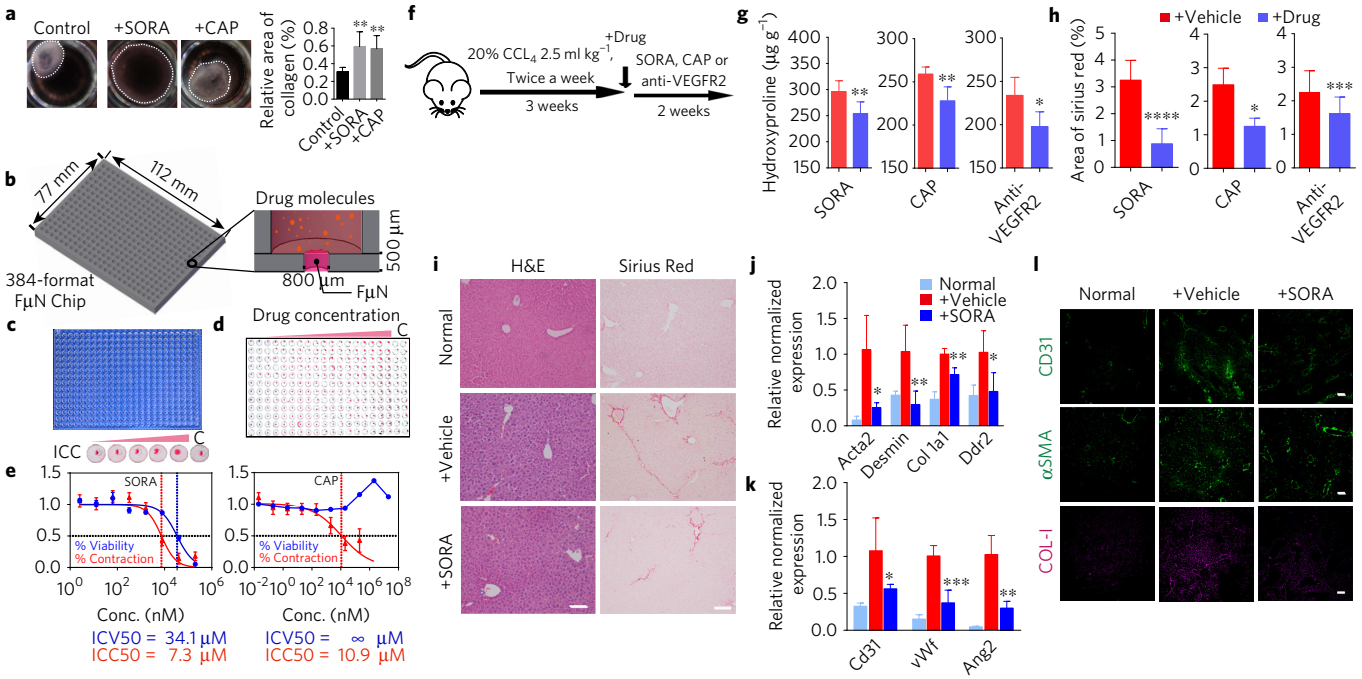

Figure 5 | Anti-angiogenesis treatment in early-stage liver fibrosis. a, *In vitro* drug testing based on early-stage FμNs by quantification of collagen contraction after drug treatment. ($n=7$, one-way ANOVA, $^{**}P=0.0027$, $P=0.0055$, respectively). **b**, Demonstration of 384 miniaturized-FμN chip for high-throughput drug testing. **c**, Photo of empty microfabricated 384-format chip. **d**, Images of the 384 miniaturized-FμN chip after administration of SORA for 48 h. **e**, Drug testing of SORA and CAP showing different ICV50 and ICC50. The data are shown as mean ± s.e.m. ($n>12$ in each data point). **f**, Schematic representation of early-stage liver fibrosis induction in C57BL/6 mice by 3 weeks of CCl_4 injection (i.p., twice per week), followed by 2 weeks of vehicle, SORA or CAP or VEGFR2 neutralizing antibody (DC101) treatment ($n=5$ in each group). **g**,**h**, Therapeutic effects of anti-angiogenesis drugs on early-stage liver fibrosis were summarized according to quantification of hydroxyproline and Sirius red (two-tailed *t*-test, $^{**}P=0.0180$, $^{**}P=0.0050$ and $^{*}P=0.0170$, respectively, in **g** and $^{****}P<0.0001$, $^{*}P=0.0183$ and $^{***}P=0.0002$, respectively, in **h**). **i**, Representative images of Haemotoxylin and Eosin (H&E) and Sirius red staining of livers from normal liver, 2-week vehicle and 2-week SORA treatment groups. Scale bar, 100 μm. **j**, Relative expression of fibrosis-related genes in normal liver, vehicle and SORA treatment groups (one-way ANOVA, $^{*}P=0.0135$, $^{**}P=0.0067$, $^{**}P=0.0056$ and $^{*}P=0.0122$, respectively). **k**, Relative expressions of sinusoid angiogenesis-related genes (one-way ANOVA, $^{*}P=0.0286$, $^{***}P=0.0006$ and $^{**}P=0.0018$, respectively). **l**, Immunofluorescent staining for collagen I (magenta), CD31 (green), and αSMA (green) of livers from different groups. Scale bar, 100 μm. Data are expressed as mean ± s.d., 5 mice in each group were included in analysis.

Histopathological examination revealed the reversal of disturbed hepatic lobules with fibroplasia in the treatment group compared to the vehicle group (Fig. 5i and Supplementary Fig. 12a,f). Reduction of fibrosis was further confirmed by downregulation of fibrosis hallmark genes (Fig. 5j and Supplementary Fig. 12b,g). Such beneficial effects may be due to the decrease in vasculature, as shown by reduced $CD31^{+}$ regions and decreased angiogenesis-related gene expression in the treatment group (Fig. 5k,l and Supplementary Fig. 12c–e,h–j). Accordingly, it verified the therapeutic efficacy of targeting sinusoid angiogenesis in early-stage liver fibrosis.

Anti-angiogenesis therapy to late-stage liver fibrosis

Late-stage fibrosis treatment has been a long-standing challenge where scars enriched in extensively crosslinked matrix components such as fibrillar collagen were formed[39]. To test the efficacy of anti-angiogenesis therapy in late-stage fibrosis treatment, SORA was administered to both *in vitro* and *in vivo* models (Fig. 6a,b). Collagen condensation was not attenuated after SORA treatment for the pre-remodelled FμNs *in vitro* model (Fig. 6a). SORA was not effective in treating late-stage fibrotic mice either (Fig. 6b–f). Reduction of $CD31^{+}$ staining (Fig. 6g) and angiogenesis-related genes (Fig. 6j) implied that SORA could still attenuate vasculature in late-stage fibrosis. However, SORA showed no therapeutic effect or even worsened late-stage fibrosis, as shown by increased αSMA expression and collagen fibre accumulation (Fig. 6g–i and Supplementary Fig. 13a–c). Similarly, CAP treatment showed no beneficial effect on late-stage liver fibrosis (Supplementary Fig. 14a–e). The failure of anti-angiogenesis therapy inspired us to explore an alternative strategy for late-stage fibrosis treatment by directly targeting the ECM components.

Anti-collagen condensation in late-stage liver fibrosis

β-aminopropionitrile (BAPN) is a small molecule inhibitor of the collagen crosslinking enzyme, lysyl oxidase (LOX)[40], which was explored for the treatment of late-stage liver fibrosis. BAPN could significantly reduce collagen fibril condensation *in vitro* (Fig. 6a and Supplementary Fig. 11d). When applied in late-stage fibrotic mice, a significant reduction of fibrosis could be achieved after a 2-week treatment (Fig. 6k–n). A dramatic reduction in αSMA^{+} activated HSCs and disruption of condensed collagen fibres were also observed after BAPN treatment (Fig. 6o–q and Supplementary Fig. 15). These results implied that targeting remoulded ECM could be an effective therapy for late-stage liver fibrosis and that therapeutic interventions to liver fibrosis should be in a stage-specific manner (see Supplementary Discussion).

Here by mimicking the stiffened ECM lining sinusoids in fibrotic liver, we validated that mechanobiologically modulated angiogenesis within FμNs resembled pathological sinusoid angiogenesis *in vivo*. We discovered that the featured sinusoid angiogenesis in early-stage liver fibrosis could only be recapitulated on substrate stiffnesses ranging from 140 to 610 Pa, which can

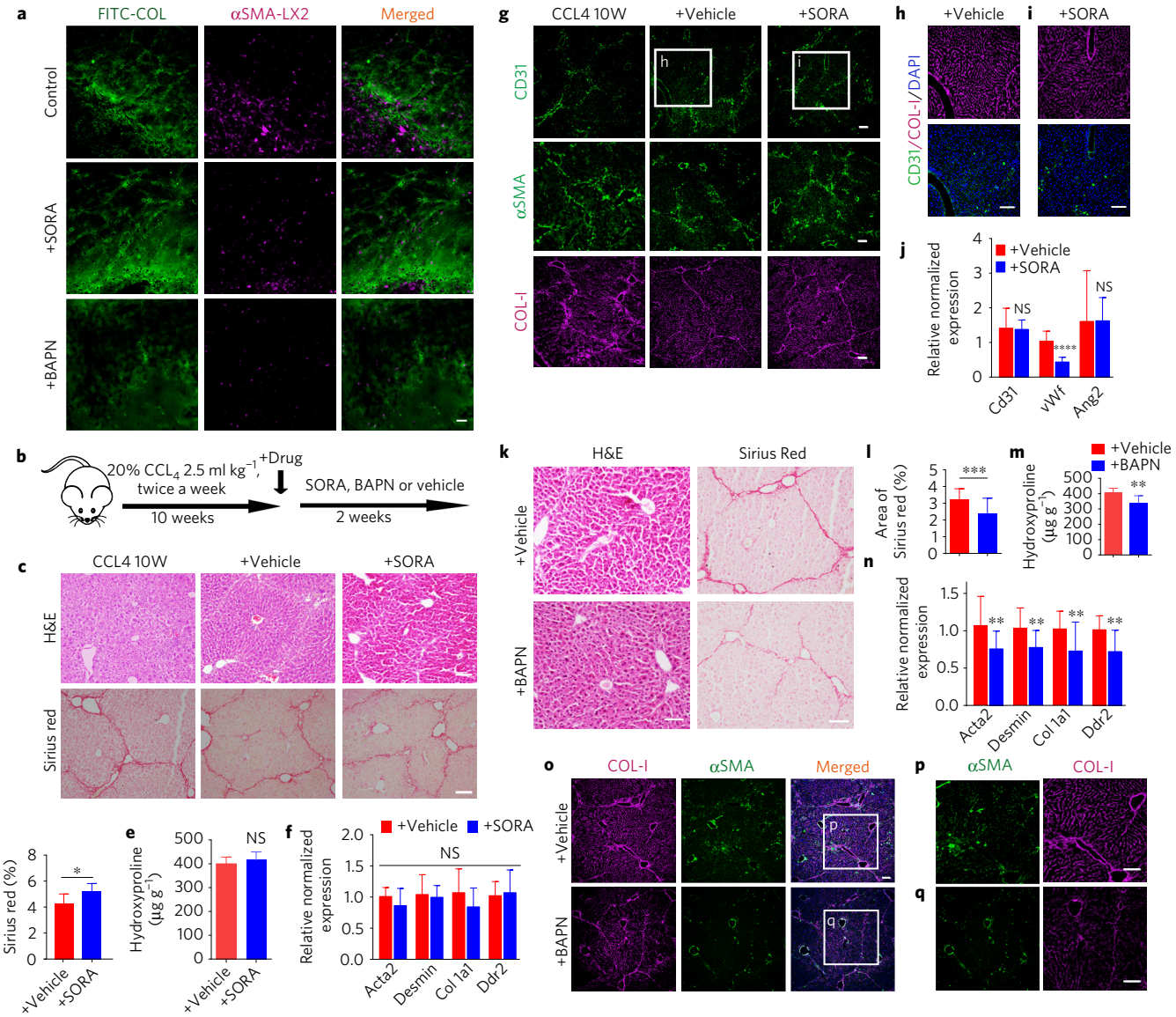

Figure 6 | Treatment of late-stage liver fibrosis by targeting vasculature and condensed collagen fibres. a, *In vitro* drug testing based on pre-remodelled FμNs with representative images of FITC-Col and activated HSCs in control and drug administration groups. Scale bar, 100 μm. **b**, Schematic representation of late-stage liver fibrosis induction in C57BL/6 mice by 10-week CCl_4 injection (i.p., twice per week) followed by 2-week vehicle, SORA or BAPN treatments ($n=6$ in each group). **c**, Representative images of H&E and Sirius red-stained sections from 10-week CCl_4 C57BL/6 mice, 2-week vehicle and 2-week SORA treatment groups. Scale bar, 100 μm. **d**, Quantitative analysis of Sirius red-positive areas ($n=12$ in each group, two-tailed *t*-test, $^{*}P=0.0302$). **e**, Therapeutic effects of SORA were evaluated by hydroxyproline quantification (two-tailed *t*-test, $P=0.2916$). **f**, Relative expression of fibrosis-related genes (two-tailed *t*-test, $P=0.1439$, $P=0.7057$, $P=0.1553$ and $P=0.7077$, respectively). **g**, Immunofluorescent staining for collagen I (magenta), CD31 (green), and αSMA (green) of liver samples from 10-week CCl_4 induction, 2-week vehicle and 2-week SORA treatment ($n=5$) groups. **h**,**i**, Enlarged immunofluorescent images of fibrotic liver in vehicle (**h**) and SORA (**i**) groups. Scale bar, 100 μm. **j**, Relative expression of sinusoid angiogenesis-related genes (two-tailed *t*-test, $P=0.8644$, $^{****}P<0.0001$ and $P=0.9738$, respectively). **k**, Representative H&E and Sirius red-stained liver tissue from 2-week vehicle and 2-week BAPN treatment groups. Scale bar, 100 μm. **l**, Quantitative analysis of Sirius red-positive areas ($n=12$ in each mouse, two-tailed *t*-test, $^{***}P=0.0002$). **m**, Therapeutic effects of BAPN evaluated by hydroxyproline quantification (two-tailed *t*-test, $^{**}P=0.0066$). **n**, Relative expression of fibrosis-related genes (two-tailed *t*-test, $^{**}P=0.0063$, $^{**}P=0.0062$, $^{**}P=0.00962$ and $^{**}P=0.0034$, respectively). **o**, Immunofluorescent images for collagen I (magenta), αSMA (green) and nuclear (blue) of livers. Scale bar, 100 μm. **p**,**q**, Enlarged immunofluorescent images of fibrotic livers in vehicle (**p**) and BAPN (**q**) groups showed the reduction of αSMA expression and disruption of collagen fibres in the BAPN group. Scale bar, 100 μm. All data are expressed as mean ± s.d., 6 mice in each group were included in analysis.

generate a mechanical force leading to collagen fibril condensation through integrin. Subsequently, the remodelled collagen fibres can function as mechanical transducer to activate HSCs through the DDR2-JAK2/PI3K/AKT-MYOCD pathway (see Supplementary Discussion). Collagen remodelling and HSC activation gradually declined as the substrate stiffness increased, highlighting the feasibility of applying mechanobiological regulation to mimic different pathological stages.

At least three factors might be involved in HSC activation mediated by mechanotransduction during collagen condensation, which include: direct mechanoactivation via collagen fibril stretching; mechanoactivation by condensed collagen matrix; and biochemical

activation by increased binding ligand density exposed to HSCs due to collagen condensation. We proved the contribution of direct mechanoactivation by AFM-induced mechanotransduction. Since collagen condensation leads to an increase in both mechanical (stiffness) and biochemical (binding ligand density) properties of collagen matrix, the contributions of ligand density and stiffness are mutually coupled, both of which have been previously shown to determine cell fate[41]. Due to the relative softness of remodelled FμNs (<1 kPa, Fig. 2l), we demonstrated that the increase in collagen ligand density upon remodelling plays a less significant role than collagen stiffening in mediating HSC activation (Supplementary Fig. 9d–f), similar to a previous investigation[42]. Meanwhile, collagen-transduced mechanobiological activation of fibroblasts into myofibroblastic phenotypes may be a conserved mechanism in fibrosis progression of other organs besides the liver, such as heart or lung, and matrix-transduced tensional forces may also occur in other matrix components, such as fibrin or elastin[19,43]. Finally, guided by the FμNs, we further obtained precise intervention strategies for liver fibrosis treatment targeting stage-specific fibrotic niche components (see Supplementary Discussion). This study broadens the horizons in our understanding of fibrosis progression and reveals unique insights into fibrosis interventions.

Methods

Methods, including statements of data availability and any associated accession codes and references, are available in the online version of this paper.

Received 2 November 2016; accepted 2 October 2017; published online 13 November 2017

References

1. Friedman, S. L., Sheppard, D., Duffield, J. S. & Violette, S. Therapy for fibrotic diseases: nearing the starting line. *Sci. Transl. Med.* **5,** 167sr161 (2013).
2. DiPietro, L. A. Angiogenesis and scar formation in healing wounds. *Curr. Opin. Rheumatol.* **25,** 87–91 (2013).
3. Hanumegowda, C., Farkas, L. & Kolb, M. Angiogenesis in pulmonary fibrosis: too much or not enough? *Chest* **142,** 200–207 (2012).
4. Ehling, J. *et al*. CCL2-dependent infiltrating macrophages promote angiogenesis in progressive liver fibrosis. *Gut* **63,** 1960–1971 (2014).
5. Thabut, D. & Shah, V. Intrahepatic angiogenesis and sinusoidal remodeling in chronic liver disease: new targets for the treatment of portal hypertension? *J. Hepatol.* **53,** 976–980 (2010).
6. Tugues, S. *et al*. Antiangiogenic treatment with sunitinib ameliorates inflammatory infiltrate, fibrosis, and portal pressure in cirrhotic rats. *Hepatology* **46,** 1919–1926 (2007).
7. Mejias, M. *et al*. Beneficial effects of Sorafenib on splanchnic, intrahepatic, and portocollateral circulations in portal hypertensive and cirrhotic rats. *Hepatology* **49,** 1245–1256 (2009).
8. Karimian, G. *et al*. Attenuation of hepatic fibrosis through captopril and enalapril in the livers of bile duct ligated rats. *Biomed. Pharmacother.* **62,** 312–316 (2008).
9. Patsenker, E. *et al*. Pharmacological inhibition of integrin αvβ3 aggravates experimental liver fibrosis and suppresses hepatic angiogenesis. *Hepatology* **50,** 1501–1511 (2009).
10. Yang, L. *et al*. Vascular endothelial growth factor promotes fibrosis resolution and repair in mice. *Gastroenterology* **146,** 1339–1350.e1 (2014).
11. Kantari-Mimoun, C. *et al*. Resolution of liver fibrosis requires myeloid cell-driven sinusoidal angiogenesis. *Hepatology* **61,** 2042–2055 (2015).
12. Garcia-Tsao, G., Friedman, S., Iredale, J. & Pinzani, M. Now there are many (stages) where before there was one: in search of a pathophysiological classification of cirrhosis. *Hepatology* **51,** 1445–1449 (2010).
13. Schaffner, F. & Poper, H. Capillarization of hepatic sinusoids in man. *Gastroenterology* **44,** 239–242 (1963).
14. Xie, G. *et al*. Role of differentiation of liver sinusoidal endothelial cells in progression and regression of hepatic fibrosis in rats. *Gastroenterology* **142,** 918–927.e6 (2012).
15. DeLeve, L. D. Liver sinusoidal endothelial cells in hepatic fibrosis. *Hepatology* **61,** 1740–1746 (2015).
16. Rockey, D. C. Vascular mediators in the injured liver. *Hepatology* **37,** 4–12 (2003).
17. Duscher, D. *et al*. Mechanotransduction and fibrosis. *J. Biomech.* **47,** 1997–2005 (2014).
18. Kilarski, W. W. *et al*. Biomechanical regulation of blood vessel growth during tissue vascularization. *Nat. Med.* **15,** 657–664 (2009).
19. Korff, T. & Augustin, H. G. Tensional forces in fibrillar extracellular matrices control directional capillary sprouting. *J. Cell Sci.* **112,** 3249–3258 (1999).
20. Bishop, P. N. The role of extracellular matrix in retinal vascular development and preretinal neovascularization. *Exp. Eye Res.* **133,** 30–36 (2015).
21. Kolodney, M. S. & Wysolmerski, R. B. Isometric contraction by fibroblasts and endothelial cells in tissue culture: a quantitative study. *J. Cell Biol.* **117,** 73–82 (1992).
22. Prasain, N. & Stevens, T. The actin cytoskeleton in endothelial cell phenotypes. *Microvasc. Res.* **77,** 53–63 (2009).
23. Melgar-Lesmes, P. *et al*. Vascular endothelial growth factor and angiopoietin-2 play a major role in the pathogenesis of vascular leakage in cirrhotic rats. *Gut* **58,** 285–292 (2009).
24. Huynh, J. *et al*. Age-related intimal stiffening enhances endothelial permeability and leukocyte transmigration. *Sci. Transl. Med.* **3,** 112ra122 (2011).
25. Tornavaca, O. *et al*. ZO-1 controls endothelial adherens junctions, cell–cell tension, angiogenesis, and barrier formation. *J. Cell Biol.* **208,** 821–838 (2015).
26. Zhao, X. & Guan, J.-L. Focal adhesion kinase and its signaling pathways in cell migration and angiogenesis. *Adv. Drug Deliv. Rev.* **63,** 610–615 (2011).
27. Wynn, T. A. Cellular and molecular mechanisms of fibrosis. *J. Pathol.* **214,** 199–210 (2008).
28. Krizhanovsky, V. *et al*. Senescence of activated stellate cells limits liver fibrosis. *Cell* **134,** 657–667 (2008).
29. Narine, K. *et al*. Growth factor modulation of fibroblast proliferation, differentiation, and invasion: implications for tissue valve engineering. *Tissue Eng.* **12,** 2707–2716 (2006).
30. Weng, S., Shao, Y., Chen, W. & Fu, J. Mechanosensitive subcellular rheostasis drives emergent single-cell mechanical homeostasis. *Nat. Mater.* **15,** 961–967 (2016).
31. Wang, Y. *et al*. Visualizing the mechanical activation of Src. *Nature* **434,** 1040–1045 (2005).
32. Ouyang, M., Sun, J., Chien, S. & Wang, Y. Determination of hierarchical relationship of Src and Rac at subcellular locations with FRET biosensors. *Proc. Natl Acad. Sci. USA* **105,** 14353–14358 (2008).
33. Ikeda, K. *et al*. Discoidin domain receptor 2 interacts with Src and Shc following its activation by type I collagen. *J. Biol. Chem.* **277,** 19206–19212 (2002).
34. Pellicoro, A., Ramachandran, P., Iredale, J. P. & Fallowfield, J. A. Liver fibrosis and repair: immune regulation of wound healing in a solid organ. *Nat. Rev. Immunol.* **14,** 181–194 (2014).
35. Olaso, E. *et al*. DDR2 receptor promotes MMP-2-mediated proliferation and invasion by hepatic stellate cells. *J. Clin. Invest.* **108,** 1369–1378 (2001).
36. Leitinger, B. Discoidin domain receptor functions in physiological and pathological conditions. *Int. Rev. Cell Mol. Biol.* **310,** 39–87 (2014).
37. Payne, L. S. & Huang, P. H. Discoidin domain receptor 2 signaling networks and therapy in lung cancer. *J. Thorac. Oncol.* **9,** 900–904 (2014).
38. Abdalla, M., Goc, A., Segar, L. & Somanath, P. R. Akt1 mediates α-smooth muscle actin expression and myofibroblast differentiation via myocardin and serum response factor. *J. Biol. Chem.* **288,** 33483–33493 (2013).
39. Sohrabpour, A. A., Mohamadnejad, M. & Malekzadeh, R. Review article: the reversibility of cirrhosis. *Aliment. Pharmacol. Ther.* **36,** 824–832 (2012).
40. Barry-Hamilton, V. *et al*. Allosteric inhibition of lysyl oxidase-like-2 impedes the development of a pathologic microenvironment. *Nat. Med.* **16,** 1009–1017 (2010).
41. Chaudhuri, O. *et al*. Extracellular matrix stiffness and composition jointly regulate the induction of malignant phenotypes in mammary epithelium. *Nat. Mater.* **13,** 970–978 (2014).
42. Engler, A. *et al*. Substrate compliance versus ligand density in cell on gel responses. *Biophys. J.* **86,** 617–628 (2004).
43. Simonetto, D. A. *et al*. Chronic passive venous congestion drives hepatic fibrogenesis via sinusoidal thrombosis and mechanical forces. *Hepatology* **61,** 648–659 (2015).

Acknowledgements

We would like to acknowledge the sequencing core facility, NIKON Biological Imaging Center, Animal Core Facility and Center of Biomedical Analysis at Tsinghua University for technical assistance. This work is financially supported by the National Natural Science Foundation of China (81522022) and National Key R&D Program of China (2017YFA0104901).

Author contributions

L.L., Z.Y. and Y.D. conceived and designed the experiments; L.L. conducted the *in vitro* FμN experiments with help from H.Z., L.Zhu and B.W.; H.Y., B.W. and L.Zhou helped to establish the hydrogel system and performed the AFM experiments, while Y.S. and T.X. provided technical support; D.L. helped in flow analysis; Z.Y. and L.L. designed and performed the mouse experiments and data processing; Bioinformatics analysis was performed by L.L. and Y.X.; W.H. and C.H. provided clinical consultation; L.L., Z.Y. and Y.D. wrote the manuscript, which W.H., C.H., H.Y., X.Y. helped to revise; Y.D. is the principal investigator of the supporting grants.

Additional information

Supplementary information is available in the online version of the paper. Reprints and permissions information is available online at www.nature.com/reprints. Publisher's note: Springer Nature remains neutral with regard to jurisdictional claims in published maps and institutional affiliations. Correspondence and requests for materials should be addressed to Y.D.

Competing financial interests

The authors declare no competing financial interests.

Methods

Animal experiments. All animal experiments were kept to a strict protocol approved by the Animal Ethics Committee of the Center of Biomedical Analysis (IACUC), Tsinghua University, which is accredited by AAALAC (Association for Assessment and Accreditation of Laboratory Animal Care International).

Cell culture and primary cell isolation. Human primary liver sinusoidal endothelial cells (LSECs) were a kind gift from L. Zhang's lab (Tsinghua University, Beijing, China), which were bought from ScienCell. LSECs were characterized through immunofluorescent staining of vWf, Factor VIII and CD31, human hepatic stellate cell line (LX-2) was bought from Xiangya Hospital of Centre-South University and further characterized by αSMA, DDR2 and Vimentin staining. All cell lines were tested negative for mycoplasma contamination. Cells were maintained in Dulbecco's Modified Eagle Medium (DMEM) (Wisent) with 10% Fetal Bovine Serum (FBS) and 1% penicillin–streptomycin (Wisent).

Primary liver sinusoidal endothelial cells and hepatic stellate cells were isolated from 8-week-old male C57BL/6 mice using a modified protocol of *in situ* collagenase digestion through the portal vein[44]. Briefly, after perfusion and collagenase IV (Life Technologies) digestion, hepatocytes were eliminated through centrifugation at 50*g* for 5 min twice. The supernatant containing non-parenchymal cells was then centrifuged at 300*g* for 10 min at 4 °C. The resulting pellet was re-suspended in RPMI 1640 (Wisent) medium and centrifuged at 1,200*g* for 25 min through a 25%/50% percoll gradient (GE). The supernatant containing HSCs was collected for fluorescence-activated cell sorting (FACS) (Aria Cell Sorter, BD). The interface at the 25%/50% percoll gradient, containing Kupffer cells and sinusoidal endothelial cells, was placed in an acid-washed glass Petri dish and incubated at 37 °C for 15 min. Non-adherent liver sinusoidal endothelial cells were then collected and replated in a culture dish. Medium was changed after 1 h to further eliminate the unattached cells. Primary LSECs isolated from fibrotic mice (3 weeks or 10 weeks of CCL_4 induction) were directly harvested using TRIzol reagent after 2 h attachment. Mouse LSECs were characterized by CD31 staining. Mouse HSCs were characterized by the auto-florescence of retinoids and αSMA staining. Primary LSECs were maintained in ECM medium (Sciencell) and primary HSCs were maintained in DMEM (Wisent) with 10% FBS and 1% penicillin–streptomycin solution (Wisent) for further experiments.

Human liver sample. Informed consent was obtained from all patients. This study was approved by the Institutional Review Board (IRB) of the School of Medicine, Tsinghua University. Human liver tissue specimens were obtained from distant non-cancerous tissues of liver-cancer patients with different stages of liver fibrosis characterized by H&E staining ($n=6$). Briefly, human liver tissue samples were frozen at −80 °C immediately after surgery, then specimens were further fixed in 10% neutral buffered formalin for 24 h according to routine procedures and embedded in optimal cutting temperature (OCT) compound (Leica) for further experiment.

2D substrate fabrication and stiffness measurement. 2D substrates with controlled stiffness were fabricated using PEG hydrogel and PDMS. As reviewed recently[45], PEG hydrogels are usually used to realize substrate stiffness in the range from pascals to kilopascals, while PDMS elastomer should be chosen for substrate stiffness within the range from kilopascals to megapascals, with a glass coverslip to represent stiffness above gigapascals.

Preparation of 2D PEG hydrogel substrate was modified from previous studies[46,47]. Briefly, PEGDA precursor solution consisting of 10% PEGDA 4000 (w/v), 0.5% photoinitiator I2959 (w/v) and 0.5% NAS (w/v) in cold phosphate-buffered saline (PBS, pH = 8.0) was dropped onto the TMSPMA-treated coverslip to form hydrogel by photo-crosslinking upon exposure to ultraviolet radiation (20 mW cm^{-2}, OmniCure SERIES 1500, Excelitas Technologies). The PEG-hydrogel-loaded coverslip can perfectly fit into 48-well microplates (NEST) for cell culture. To further rule out the variance in chemical composition, we modified the coverslip with a thin layer of PEGDA hydrogel via surface-initiated photo-polymerization[48]. PDMS substrates with stiffness in the kilopascal to megapascal range were fabricated according to a previously established protocol[49]. All the substrates were coated at 4 °C overnight with 0.1% gelatin (sigma) dissolved in diH_2O, which was proved to be at similar coated concentrations on the substrate surfaces with different stiffness[46]. Stiffness measurement by AFM has been described previously[46]. Hydrogels were crosslinked on TMSPMA-modified 25 mm-diameter coverslips prior to indentation. The force versus indentation curves from each measurement were analysed by JPKSPM Data Processing software using the Hertz model to obtain the Young's modulus of each hydrogel.

Establishment of FμNs. LSECs were grown to 90% confluence before harvest. 5×10^4 human LSECs or 1×10^5 primary mouse LSECs were seeded on hydrogel surfaces of different stiffness (200 Pa, 610 Pa and coverslip) for 12 h at 37 °C in an incubator with 5% CO_2. Then human HSC cell line LX-2 or primary mouse HSCs were suspended in type I collagen (BD) prepared according to the manufacturer's instructions (5×10^5 cells ml^{-1} for LX-2 or 1×10^6 cells ml^{-1} for primary mouse HSC, 2 mg ml^{-1} collagen type I). 120 μl of gel suspension with cells was applied into 48-well microplates, on top of the LESCs cultured on PEG hydrogel of different stiffness. 300 μl cell culture medium was then added to each well after a 15 min polymerization of collagen gel at 37 °C. Remodelling of collagen gel in different FμNs was examined 12 h later. Images of different FμNs before and after contraction were analysed by Image J to obtain the relative area change (%), which is the ratio of gel area after contraction to gel area before contraction. Young's moduli of FμNs after remodelling were measured by AFM as described in the previous section.

RNA-Seq. As represented in Fig. 2a, primary LSECs were isolated from normal C57/BL6 mice. After culture *in vitro* for 48 h, cells were harvested and replated on a 200 Pa substrate or coverslip for 24 h before RNA extraction. Pathological LSECs were isolated from early-stage fibrotic mice (3 weeks of CCL_4 induction) and late-stage fibrotic mice (10 weeks of CCL_4 induction). Total RNA of primary LSECs *in vitro* and *in vivo* was extracted using TRIZOL reagent. After library construction and sequencing, we obtained 106.7 M 22.2M, 29.4M, 22.2M, 38.0M raw reads for normal, 200 Pa, COV, 3W and 10W, respectively. Clean reads were mapped to the mouse genome sequence (ftp://ftp.ncbi.nlm.nih.gov/genomes/refseq/vertebrate_mammalian/Mus_musculus/latest_assembly_versions/GCF_000001635.25_GRCm38.p5) using STAR[50]. Gene expression level was quantified using DEGseq[51]. The genes with counts greater than 10, at least twofold change in expression, and *q*-values less than 0.01 were considered to be differentially expressed. Hierarchical clustering was performed in both the gene and the sample dimensions and drawn as a bi-clustering heatmap. To demonstrate the gene expression profiles of LSECs during fibrosis progression, DEGs changed in 3W and 10W (compared to normal respectively) were included in the analysis, and signalling related to fibrosis and angiogenesis was listed according to the CPM (counts per million, *Z*-score normalization). To compare the similarity of LSECs *in vitro* and *in vivo*, genes significantly changed both in early-(200 Pa, 3W group compared to the normal group respectively) and late-stage (COV, 10W group compared to the normal group respectively) LSECs were used to identify the pathways and specific genes. Pathways and related genes involved in angiogenesis are listed according to $\log_2$FC in Fig. 2d,e and Supplementary Fig. 6.

Reporter system. Human αSMA gene promoter (2.1 kb) was cloned into pENTR 5′-TOPO. Then the cloned plasmids were recombined with D-TOPO-mCherry and p2K7-bsd using Gateway LR Clonase II Enzyme mix (Invitrogen) to create final reporter lentivirus vector as previously reported[52]. The pENTR/D-TOPO and p2K7-bsd plasmids were generous gifts from K. Kee (Tsinghua University, Beijing, China). Cells were transduced with lentivirus and selected with blasticidin (2 μg ml^{-1}) in culture for 3 days to ensure stable integration. p2K7-CMV-mCherry, TagBFP-Tubulin was also used to label LSECs in experiments, and fluorescence positive cells were isolated through cell sorting (BD).

FμN digestion and flow analysis. Collagenase type I (Life Technologies) was dissolved in Hank's Balanced Salt Solution (HBSS) to a final concentration of 200 U ml^{-1}. FμNs were washed in 1 ml HBSS before digestion. Then 300 μl collagenase type I was added and incubated at 37 °C for 5 min to ensure complete dissolution. FμNs were then washed with PBS three times to collect cells in FμNs for further analysis. Cells carrying αSMA-GFP reporter were directly analysed by flow cytometry (BD LSRFortessa). For proliferation analysis, cells in FμNs were stained with Ki-67 antibody for 30 min and washed with PBS three times. Only mCherry negative cells were included in the analysis (LSEC carrying CMV-mCherry gene).

Gene expression analysis. Cells, FμNs or tissue samples were homogenized in TRIZOL reagent (Life Technologies) before RNA extraction following the manufacturer's instructions. cDNA was synthesized from 1 μg of DNA-free total RNA using Reverse Transcriptase M-MLV (Taraka). Gene-specific transcription analysis was determined using AceQ qPCR SYBR Green Master Mix (Vazyme) and CFX96 machine (Bio-Rad), with triplicates for each sample. All genes were normalized to GAPDH. Primers are listed in Supplementary Table 2.

Live-cell imaging. Time-lapse recordings were obtained by means of a Nikon Eclipse Ti-S microscope in a live-imaging chamber at 37 °C with a CO_2 supply, as previously described[46,47].

Paracrine factor/mechanical factor characterization. LSECs cultured on 200 Pa surfaces for 12 h were fixed in 4% paraformaldehyde for 15 min at room temperature, and washed using PBS three times (15 min each) to make sure no residual PFA remained. Medium collected from LSECs previously cultured on 200 Pa surfaces for 24 h was then added. To make a 'Transwell', a 48-well microplate was manually pierced between neighbouring wells using a needle to enable free diffusion of soluble factors. To collect dead cells, cells were trypsinized and fixed

with 4% paraformaldehyde at room temperature for 10 min, then washed with PBS three times (15 min each) to make sure no residual PFA remained. Cell membranes remained intact after such treatment, as observed with a microscope. To inhibit cell contractility and migration, cells were treated with 25 μM (-)-Blebbistatin (Cayman) for 8 h before being overlaid by collagen hydrogel.

Cell stretching experiment. The cell stretching experiment was performed on a STREX mechanical strain instrument (B-Bridge International). Briefly, WT-LX-2 or shDDR2-LX-2 cells were suspended in collagen hydrogel and gelated in a PDMS chamber provided by the strain instrument. After 4 h of cell attachment, the chamber was then loaded with a 4% stretching for 12 h before stretching at 10% for another 12 h. Samples were collected for further gene expression or western blot analysis. 10 μM PI3K inhibitor (ZSTK474), 500 nM DDR2 inhibitor (DDR1-IN-1), 10 μg ml^{-1} AKT inhibitor (MK-2206 2HCl), 0.5 μM JAK2 inhibitor (INCB018424) (Selleck Chemicals) were individually added into the chamber for 24 h treatment. Afterwards, cells were harvested for further analysis.

Mouse anterior chamber angiogenesis model. The mouse anterior chamber angiogenesis model is described in Fig. 3k. AIM (angiogenesis induction material) was fabricated as follows: PEGDA-based microscaffold was fabricated as previously described[53] and 1 μl bFGF (100 ng μl^{-1}) was absorbed into the microscaffold. The bFGF-loaded microscaffold was then freeze-dried. The dried bFGF-loaded microscaffold was then absorbed with 1% alginate pre-polymer solution and crosslinked in 100 mM $CaCl_2$ for 10 min for controlled release of bFGF before implantation. The implantation protocol was modified from a previous study[54]. Briefly, mouse eyes were exposed for implantation after anaesthetization and for an incision made using a surgical knife under a stereomicroscope. Then, one AIM or control material was implanted into the anterior chamber of the eyes using forceps. A drop of eye-drop was applied on the eye to prevent desiccation. After 3 days of angiogenesis induction, FITC-collagen and αSMA-mCherry LX-2 mixture was injected into the mouse anterior chamber via a 31G modified needle using a programmable syringe pump (WPI). After another 3 days, remodelling of the mouse eyes was imaged under confocal laser scan microscopy (FV1000MPE, Olympus).

Atomic force microscope (AFM)-applied mechanical stimulation. HSCs were transfected with KRAS-SRC biosensor, which was a gift from Y. Wang (Addgene plasmid # 78302), and were previously used to visualize the mechanical activation of SRC[31,32].

Mechanical stimulation of HSC at the single-cell level was achieved by the AFM module Nanowizard (JPK Instruments) where samples were mounted on an inverted fluorescence microscope (Zeiss Observer A1 stand). The silicon tipless cantilever (ARROW-TL1-50, NANOWORLD) used to indent the samples has a nominal spring constant of 0.03 N m^{-1} and was attached with a silicon microsphere (6 μm in diameter) on the cutting edge. To apply tensile force on the collagen gel, the cantilever was firstly moved to the adjacent area of a target HSC with the microsphere in contact with the upper surface of the collagen gel. Next, the cantilever was further moved down by 2–3 μm into the collagen gel. The cantilever was then stretched away from the target HSC in the horizontal direction with a tensile force of 200 nN through stretching collagen fibrils. Meanwhile, the fluorescent (ECFP) signal change of SRC biosensor in HSC was monitored during microscopy. In this process, the collagen gel contacted with the microsphere moved along with the cantilever with obvious deformation. The tensile force applied on the gel was estimated according to the displacement of the microsphere (Supplementary Fig. 9a). After 15 min, the cantilever was removed from the gel surface in the vertical direction and recording of the fluorescence signal was terminated at the same time.

Western blot. Total proteins from FμNs were extracted using RIPA lysis buffer (Beyotime) supplemented with protease inhibitors PMSF (Beyotime). Proteins were separated on polyacrylamide gels, and then transferred onto PVDF membrane (Millipore) and detected by secondary antibodies and Super-Signal West Pico Chemiluminescent Substrate (Thermo). Uncropped scans of western blots are shown in Supplementary Figs 4d and 16.

Drug administration *in vitro*. After establishment of FμNs, drugs supplemented in medium were used to inhibit early-stage tissue remodelling. Drug concentrations used were 10 mM for Captopril (Tokyo Chemical Industry) and 4 μM for Sorafenib (Solarbio). Images were taken after 12 h remodelling. For late-stage fibrotic tissue analysis, 120 μl (1×10^6 cells ml^{-1}) of LX-2 in FITC-Collagen was allowed to freely remodel in bovine serum albumin (BSA)-blocked 48 wells for 12 h. SRC inhibitor (KX2-391, 2 μM, Selleck) with no off-target effect was applied to FμNs to confirm the correlation of SRC with HSC activation. Pre-contracted collagen gels with similar area were chosen for Sorafenib or β-Aminopropionitrile Fumarate (BAPN, 10 μg ml^{-1}, Santa Cruz Biotechnology) administration for another 12 h. Images of the remodelled tissues were taken using confocal microscopy (A1RMPSi, Nikon).

***In vitro* drug testing on a 384-format miniaturized-FμN chip.** The 384-format miniaturized-FμN chip with LESCS-induced collagen condensation and HSC activation in a smaller scale was established based on a 384-format microfabricated chip, as a modification of our published protocol[55].

In brief, a mixture of LX-2 (with a density of 6.7×10^5 ml^{-1}) and Rat tail collagen I working solution (2 mg ml^{-1}) was loaded onto the cell-laden side of an assembled 384-format microfabricated chip for 1 h gelation at 37 °C, then LSECs in 11 μl ECM medium (Sciencell) (with a density of 6×10^4 ml^{-1}) were pipetted into each reservoir manually or using a liquid handler (Apricot), so as to make the ratio of LX-2 and LSEC equal to 1:2 for each miniaturized FμN. Subsequently, the concentration gradient of drug, namely SORA, CAP, DOX, diluted in 11 μl ECM medium was applied to the chip. 48 h later, the inhibitory concentration of viability (ICV) curve and the inhibitory concentration of contraction (ICC) curve were plotted according to our published protocol[55]. As an alternative approach to induce collagen condensation and HSC activation in FμNs, LESCs could be first mechanically primed on PEG hydrogel substrates with a stiffness of 200 Pa for 24 h, and subsequently harvested by trypsinization to seed on the HSCs-laden collagen gels to initiate the collagen remodelling and HSC activation (Supplementary Fig. 10).

Mouse model of liver fibrosis. Liver fibrosis of 8-week-old male C57BL/6 mice were treated with CCl_4 (2.5 ml kg^{-1} body weight; 1:4 dilution with olive oil) or with olive oil as control by intraperitoneal injection two times a week for 3 or 10 weeks. 3-week induction resulted in F2 stage fibrosis according to the METAVIR staging system, with 10-week induction resulting in more severe fibrosis (above F3 stage in METAVIR).

Antibody. Antibodies used in this study are listed in Supplementary Table 3.

Drug treatment protocol. Sorafenib or CMC was administered orally by gavage, once a day, for 2 weeks at a dose of 2 mg kg^{-1} d^{-1} in mouse with liver fibrosis. Captopril (50 mg kg^{-1} d^{-1}) was dissolved in the drinking water and was given *ad libitum* by free drinking for 2 weeks. Fresh Captopril solution was prepared every 2 days, the concentration of which was dependent on the average body weight and drinking volume of mice in each cage for 2 days. Anti-VEGFR2 antibody (5 mg kg^{-1} d^{-1}, DC101, Bio X Cell) was injected intraperitoneally once per day for 2 weeks. BAPN (100 mg kg^{-1}) or vehicle (PBS) was injected intraperitoneally once per day during treatment. Treatments began after 3 or 10 weeks when liver fibrosis was developed. After 2 weeks of treatment, all animals were euthanized under Avertin anaesthesia. Livers were removed and fixed in 10% neutral buffered formalin and then embedded in OCT for histological examination. Only the right lobe was included for comparable analysis.

Statistical analysis. Statistical analysis was performed by GraphPad Prism. Significant differences between groups were checked using one-way ANOVA following Tukey's multiple comparisons test or unpaired, two-tailed Student's *t*-test. One-way ANOVA was used when comparing three or more groups of data and Student's *t*-test was used when determining two groups of data, as indicated in the figure legend. Unless indicated otherwise, all quantification data are presented as mean values ± standard deviation (s.d.). Experiments have at least three independent replicates.

Data availability. The authors declare that the data supporting the findings of this study are available within the paper and its supplementary information files.

References

44. Mederacke, I. *et al*. High-yield and high-purity isolation of hepatic stellate cells from normal and fibrotic mouse livers. *Nat. Protoc.* **10,** 305–315 (2015).
45. Yang, Y., Wang, K., Gu, X. & Leong, K. W. Biophysical regulation of cell behavior—cross talk between substrate stiffness and nanotopography. *Engineering* **3,** 36–54 (2017).
46. Wang, B. *et al*. Substrate stiffness orchestrates epithelial cellular heterogeneity with controlled proliferative pattern via E-cadherin/β-catenin mechanotransduction. *Acta Biomater.* **41,** 169–180 (2016).
47. Zhao, H. *et al*. Microengineered *in vitro* model of cardiac fibrosis through modulating myofibroblast mechanotransduction. *Biofabrication* **6,** 045009 (2014).
48. Kızılel, S., Sawardecker, E., Teymour, F. & Pérez-Luna, V. H. Sequential formation of covalently bonded hydrogel multilayers through surface initiated photopolymerization. *Biomaterials* **27,** 1209–1215 (2006).
49. Gutekunst, S. B. *et al*. Influence of the PDMS substrate stiffness on the adhesion of Acanthamoeba castellanii. *Beilstein J. Nanotech.* **5,** 1393–1398 (2014).
50. Dobin, A. *et al*. STAR: ultrafast universal RNA-seq aligner. *Bioinformatics* **29,** 15–21 (2013).
51. Wang, L. *et al*. DEGseq: an R package for identifying differentially expressed genes from RNA-seq data. *Bioinformatics* **26,** 136–138 (2010).

52. Kee, K. *et al*. Human DAZL, DAZ and BOULE genes modulate primordial germ cell and haploid gamete formation. *Nature* **462,** 222–225 (2009).
53. Zeng, Y. *et al*. Injectable microcryogels reinforced alginate encapsulation of mesenchymal stromal cells for leak-proof delivery and alleviation of canine disc degeneration. *Biomaterials* **59,** 53–65 (2015).
54. Speier, S. *et al*. Noninvasive high-resolution *in vivo* imaging of cell biology in the anterior chamber of the mouse eye. *Nat. Protoc.* **3,** 1278–1286 (2008).
55. Zhao, H. *et al*. Bi-content micro-collagen chip provides contractility-based biomechanical readout for phenotypic drug screening with expanded and profiled targets. *Lab Chip* **15,** 3481–3494 (2015).